Understanding the consolidation mechanism of selective laser sintering/powder bed selective laser process of ceramics: Hydroxyapatite case

Asif Ur Rehman, Pedro Navarrete-Segado, Metin Salamci, Christine Frances, Mallorie Tourbin, David Grossin

Author version of the paper:

Understanding the Consolidation Mechanism of Selective Laser Sintering / Powder Bed Selective Laser process of Ceramics: Hydroxyapatite Case

Asif UR REHMAN, Pedro NAVARRETE-SEGADO, Metin U. SALAMCI, Christine FRANCES, Mallorie TOURBIN, David GROSSIN

***Published in Rapid prototyping journal*, 01 May 2024, Vol. 30, Issue 4, pages 677 - 695**

- **ISSN:** 13552546
- **DOI:** 10.1108/RPJ-04-2023-0128
- **Publisher:** EMERALD GROUP PUBLISHING LIMITED; Emerald Publishing Limited

This project has received funding from the European Union's Horizon 2020 research and innovation programme under the Marie Skłodowska-Curie grant agreement No 764935.

Received 8 April 2023, Revised 27 December 2023, Accepted 4 February 2024

Understanding the Consolidation Mechanism of Selective Laser Sintering / Powder Bed Selective Laser process of Ceramics: Hydroxyapatite Case

Asif UR REHMAN,[1] Pedro NAVARRETE-SEGADO,[2,3] Metin U. SALAMCI,[4,5] Christine FRANCES,[2] Mallorie TOURBIN,[2] David GROSSIN,[3]

[1] ERMAKSAN, Bursa, 16065, Turkey

[2] Laboratoire de Génie Chimique, Université de Toulouse, CNRS, 4 Allée Émile Monso, 31432 Toulouse Cedex 4, France

[3] CIRIMAT, Université de Toulouse, Toulouse-INP, UPS, CNRS, 4 Allée Émile Monso, 31432 Toulouse Cedex 4, France

[4] Department of Mechanical Engineering, Gazi University, 06570 Ankara, Turkey

[5] Additive Manufacturing Technologies Application and Research Center- EKTAM, Gazi University, 06560 Ankara, Turkey

Abstract:

Design/methodology/approach: Additive manufacturing (AM) has revolutionized automotive, biomedical and aerospace industries, among many others. AM provides design and geometric freedom, rapid product customization and manufacturing flexibility through its layer by layer technique. However, a very limited number of materials are printable because of rapid melting and solidification hysteresis. Melting-solidification dynamics in powder bed fusion is usually correlated with welding, often ignoring the intrinsic properties of the laser irradiation; unsurprisingly the printable materials are mostly the well-known weldable materials.

Purpose: The consolidation process and morphology evolution in ceramics-based additive manufacturing are still not well understood. As a way to better understand the ceramic Selective Laser Sintering (SLS) a dynamic three-dimensional computational model was developed to forecast thermal behavior of hydroxyapatite (HA) bioceramic.

Findings: The consolidation mechanism of HA was identified during its processing in a ceramic SLS device, then the effect of the laser energy density (LED) was studied to see how it affects the processing window. Premature sintering and sintering regimes were revealed and elaborated in detail. The full consolidation beyond sintering was also revealed along with its interaction to baseplate.

Originality/value: These findings provide important insight into the consolidation mechanism of Hydroxyapatite ceramics which will be the cornerstone for extending the range of materials in laser powder bed fusion of ceramics.

Keywords: Hydroxyapatite; Powder bed selective laser process; Powder bed fusion; Laser energy Density; Ceramic laser-powder bed fusion;

Abbreviation list

AM	Additive manufacturing
CFD	Computational fluid dynamics
HA	Hydroxyapatite
HD	Hatch distance
LED	Laser energy density
L-PBF	Laser-powder bed fusion
LP	Power of the Laser
LS	Scanning speed of the Laser
LT	Layer Thickness
MP	Multi-physics
PBSLP	Powder bed selective laser process
PSD	Powder Size Distribution
SEM	Scanning Electon Microscopy
SLS	Selective Laser Sintering

Symbols

v	Profile of the velocity
$\vec{\mathbf{P}}$	Applied pressure
μ	Viscosity of the material
$\vec{\mathbf{g}}$	Gravity function of the material
α	Coefficient of thermal expansion of the material
ρ	Density of the material
$\boldsymbol{b}$	Enthalpy of the material
k	Heat conductivity of the material
$\boldsymbol{V_F}$	Metal volume fraction inside the cell
$\boldsymbol{V_F}$ **= 0**	Cell within the mech is free of the fluid
$\boldsymbol{V_F}$ **= 1,**	Cell within the mech is fully fluid
$\boldsymbol{\omega}$	Width of melt pool

P	Beam power
η is	Absorptivity
ρ	Density
C_p	Heat capacity
V	Scanning velocity
T_m	Melting temperature
T_0	Room temperature specifies preheating level
ΔH_v	Accumulated heat of vaporization
R	Gas constant
T_v	Saturation temperature
T	Temperature of the flow
A	Powder bed's beam absorption
R_b	Laser radius
v	The scanning rate of the laser
(x_0, y_0)	Initial location of the laser beam center's
R_b,	Radius of the beam
h_c	Coefficient of convective heat transfer
q_{evap}	Heat transfer due to evaporation
σ_0	Stefan–Boltzmann constant
ε	Measure of emissivity
ω_0	Evaporation rate.
$\dot{m}$	Mass flow rate
$\vec{A}$	Area

1. Introduction

Additive manufacturing (AM) has revolutionized many industries, including construction[1], [2], biomedical [3], aerospace and to achieve design flexibility and shortened time to market [4]–[6]. Laser powder bed fusion (L-PBF) is an AM process for making parts and freeform objects in which the production layer is selectively consolidated by a high-energy laser beam following powder deposition [7], [8]. L-PBF can achieve upto 96 % density and superior mechanical characteristics for alloys in which

powder particles are melted together [9], [10]. L-PBF has an exceptional heating and cooling cycle rate, resulting in non-equilibrium conditions; novel microstructures as well as material phases are often produced throughout the process [11].

The thermal and mechanical properties of advanced ceramics make them appropriate for a wide range of sectors, including aviation, medicinal devices, semiconductor production, and power generation. As a consequence, it is evident that AM technology has to be improved to manufacture complex forms comprised of sophisticated ceramic materials [12]–[16]. It is commonly known that the L-PBF of alloys or metals operate on the same criterion as weldings [9] – for example nucleation theory or undercooling have also been employed to generate high-strength metal components [17]–[19]. However, this is not the case in ceramics where thermal cracking makes it very difficult to use melting as a preferable printing method [20], [21]. The phenomenon that occurs during the densification of ceramics produced with a laser source hasn't been well investigated [22]–[25]. Some materials may undergo compositional changes prior to sintering/melting (sintering is defined as solid state diffusion rather than partial melting [24]), and both processes can occur as a consequence of increased temperature [24]. To avoid misusing the preceding terminology to define the approach, the term powder bed selective laser process (PBSLP) was recently suggested [16], [26].

One major challenge for the application of direct SLS into most of the ceramics is the poor absorption (close to 3-4% for oxide ceramics) of energy from fiber lasers, having wavelengths between 1030 and 1070 nm. While metals have absorption values between 60-80 percent [27]. The high young's modulus, low tensile, and large thermal expansion coefficient of most ceramic materials make them resistant to thermal shocks [16], [24], [28].

To obtain high densities and defect-free components, previous ceramic SLS experiments focused primarily on developing new ways for optimizing the laser-powder interaction. Laser absorptivity improvement through the addition of additives [20], [29], pre-heating systems [16], [30]–[32], and specific powder formulations with eutectic ceramics (i.e. $Al_2O_3/GdAlO_3/ZrO_2$) [33] are effective ways that may be used in combination.

The morphology of additively manufactured materials is strongly influenced by the size and geometry of the irradiated zone. [34], [35]. When working with SLS, it is difficult to accurately measure the size and shape of the irradiated zone under the beam [35], [36]. Some light alloys have been characterised by using tungsten nanoparticles as markers under synchrotron x-ray facilities [34]–[36] among others [37]. Due to their nature of absorpting the x-rays ceramics are impossible to directly characterise in-situ. Therefore, the consolidation or shaping mechanism of ceramics has not been revealed clearly [38]. Melting-consolidationsolidification as well as sintering have already been studied for conventional processes [39], but not for AM [40] and more specifically SLS [24].

HA is an important ceramic material for biomedical applications [24], [41]–[44]. The production of calcium phosphate scaffolds through SLS has been largely studied [24] for orthopedic implants. Scientists have used three basic SLS techniques to shape HA bioceramic particles. The first technique involves filling polymer materials with HA [45], [46]. Laser irradiation melts the polymer in the powder feedstock [47], [48], creating a polymer/ceramic composite scaffolds. Since these polymers are not eliminated following SLS, implantation might influence their characteristics or tissue regeneration [49]. A second technique uses a similar mix of polymer/ceramic components to create green body scaffolds. After pyrolysis and sintering, the bioceramic scaffold is free of the polymer [50].

The third strategy for SLS, is to increase the laser absorption of HA powder and use it directly, without the need of polymer [44]. In a prior research, within this context, a development of calcium phosphate powdered feedstock by the inclusion of varying quantities of graphite as an absorption additive was accomplished, and the powder was optimized [26]. Hydroxyapatite (HA) powder feedstocks were examined in a SLS process at various printing parameters to see how the energy density of each powder affected its printing [20]. However, the understanding of the narrow processing window still needs to be disclosed.

In this study, the underlying shaping mechanism in SLS of HA was studied. A method for tracking shaping behavior across the entire regime in SLS was developed using DEM and FVM. A high-intensity laser was used to create HA single tracks on an HA-coated substrate. For single track creation, a comprehensive investigation was carried out investigating the function of LED. Geometry, morphology, consolidation of single tracks produced at different LED values were thoroughly investigated. SLS shaping thermal behavior was also simulated using a finite volume method-based model and confirmed by experiments. We uncovered the consolidation mechanism and observed the driving factors as well as the fundamental processes throughout the consolidation domain.

2. Materials and Methods

2.1. Powder

The particle size distribution (PSD) for HA powder (Urodelia SA Company, Saint-Lys, France, product reference 206.93.003) was obtained by laser diffraction in suspension, performed in a Mastersizer MS 3000 (Malvern Panalytical®). Refractive indexes: 1.63 and 1.33 for particles and water, respectively. A complete powder flow evaluation of the present HA powder was performed in a previous work [26]. Four different static and dynamic flowability methods were used for the analysis of the following properties: Angle of repose (31 ± 1º), Hausner ratio (1.12 ± 0.02), flow rate through an orifice (275 ± 22 $kg.h^{-1}$), and flow factor coefficient (16 ± 2). The results indicated that the powder flowability was suitable for its use in any powder bed fusion process, considering it a free flowing powder. It was mainly attributed to the particle spherical shape and size distribution.

As mentioned in the introduction, fiber laser absorptance of HA powder was improved by mixing it with TIMREX® KS 44 Graphite (G) by Imerys, following a previous work procedure [26]. Carbon graphite-based filleracts as a near-infrared absorptance additive that improves the powders' laser-material interactions. Powder blends at different concentrations were prepared by pouring the powders in a controlled proportion (with 0.5 kg in total) in a mixing jar, to mechanically blend them using a Turbula shaker mixer at 42 rpm for 1 h.

2.2. Powder Modelling

The HA powder generation process was modeled. Figure 1 a) shows the spray dried HA powder (details have been provided in section 2.1) particles, while the particle size distribution has been shown in (b). The physical powder particles have been simulated in decent estimate to the scanning electron microscope (SEM) imaging and PSD. Figure (c) shows the particle obtained from simulation. The particle sizes were confirmed to be in agreement with the experimental calculations, and they matched D10, D50, and D90, respectively.

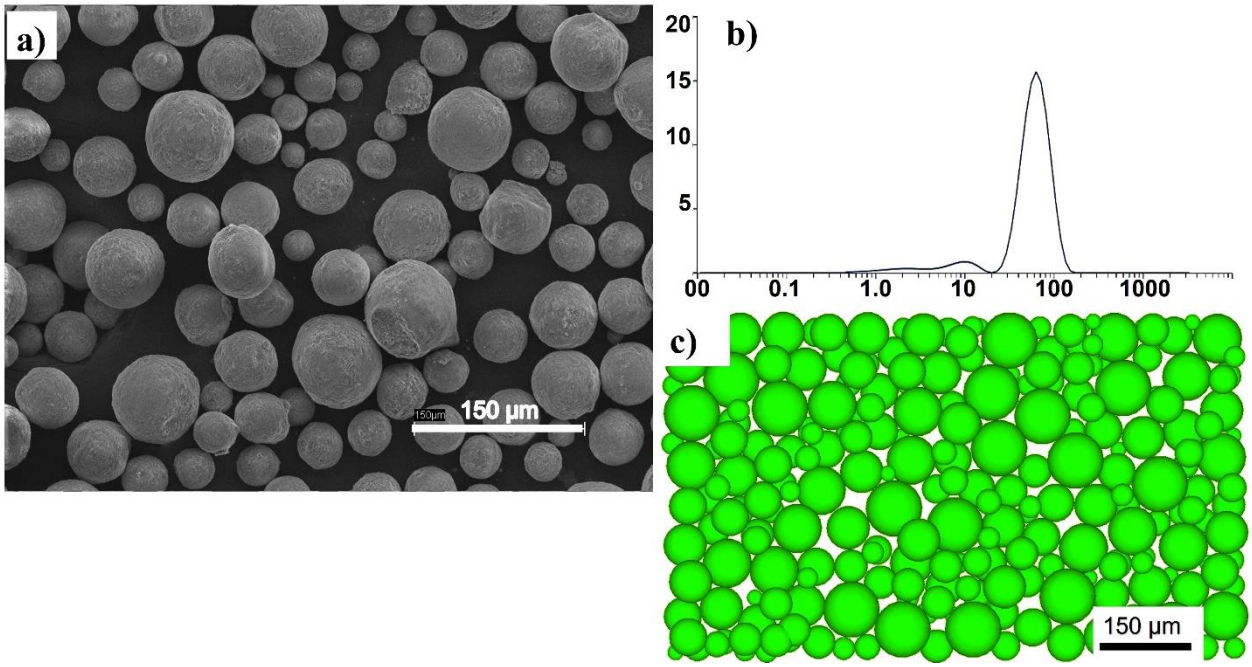

Figure 1 a) SEM image of the HA powder particles, b) Particle Size Distribution (PSD) and c) Discrete Element Modelling of the same PSD.

The FS DEM from Flow Science, USA, was utilized to represent HA powder throughout this study. Rather than treating the layer of powder as a uniform plate, a layer of powder was produced utilizing discrete microparticles. The powder bed layer thickness is 100 µm. A 100 µm layer was also deposited in the DEM model. The layer of the powder had a packing density of 65% while keeping the voids on the outer/free surface inside the block, then a 90% after eliminating them.

2.3. Modeling of Thermophysical Properties

HA powder was produced via wet-chemical coprecipitation, milling, and spray-drying process to confer it the spherical shape. The investigations made use of a HA powder that had a form that was primarily spherical in nature. with a 300% powder compression produced by the roller after powder bed settling and before laser scanning.

Temperature dependent physical properties in the CFD analysis HA were used from the literature.

SLS process involves rapid consolidation as well as solidification, which affects all of the thermo-physical properties associated.

2.4. Numerical model

A CFD approach was introduced, and implemented using discrete element modelling (DEM) and volume of fluid methods (FVM), using subprocesses. For clarity, the several factors and generalizations are considered in the investigation: (1) the consolidation throughout the field of consolidating domain is incompressible Newtonian; (2) the mass change due to ceramic evaporation is often neglected. .

In (i), (ii), and (iii), the preceding equations are then solved for energy conservation, momentum, and, mass continuity in that order [51]:

i. $\nabla \cdot \vec{\mathrm{v}} = 0$

ii. $\frac{\partial \vec{\mathrm{v}}}{\partial \mathrm{t}} + (\vec{\mathrm{v}} \cdot \nabla)\vec{\mathrm{v}} = -\frac{1}{\rho}\nabla \vec{\mathrm{P}} + \mu \nabla^2 \vec{\mathrm{v}} + \vec{\mathrm{g}}[1 - \alpha(\mathrm{T} - \mathrm{T_m})]\mathrm{g}[1 - \alpha(\mathrm{T} - \mathrm{Tm})]$

iii. $\frac{\partial h}{\partial \mathrm{t}} + (\vec{\mathrm{v}} \cdot \nabla)h = \frac{1}{\rho}(\nabla \cdot \mathrm{k}\nabla \mathrm{T})$

Wherein v represents the velocity, μ denotes viscosity, $\vec{\mathrm{P}}$ indicates pressure, α indicates coefficient of thermal expansion, h indicates specific enthalpy, $\vec{\mathrm{g}}$ represents gravity function, ρ indicates density, and k is thermal conductivity.

The volume of fluid (VOF) model makes advantage of the free surface to glean data [51], [52]. The VOF approach may be expressed as an equation (iv):

iv. $\frac{\partial V_F}{\partial t} + \nabla(\vec{v} \cdot V_F) = 0$

where V_F represents the metal HA volume fraction contained inside the cell. If V_F=1, It demonstrates that the cell is completely fluid, while V_F=0 shows that the cell is no longer filled with liquid. Quantities in the middle demonstrate the presence of a free surface across the mesh.

The difference in consolidation domain could be attributable to a number of factors, including thermo-physical properties. Because the The Rosenthal technique is dereived from the heat equation & neglects convection, evaporation, and Marangoni effect, the corresponding term in Eq. (v) for consolidation domain diameter obtained from Rosenthal equation is used to reflect the role of temperature dependent properties for consolidation domain difference [51] in heat conduction:

v. $\omega = \sqrt{\frac{8}{\pi \mathrm{e}} \cdot \frac{P\eta_{\eta n}}{\rho C_p V(T_m - T_0)}}$

Where P is beam power, η denotes absorptivity, ρ denotes density, C_p indicates thermal capacity , V indicates scanning speed , T_m represents the melting point , whereas T_0 represents the amount of pre-heating .The Rosenthal solution is generated by assuming physical properties temperature independent and the temperature dependent conductivity is utilized to evaluate consolidation domain size.

Incorporating the impacts of both recoil pressure and vapor suppression on the consolidation domain scale [51], each recoil pressure might be computed using Eq. (vi):

$$\text{vi.} \quad P_S = A \cdot exp\left\{B\left(1 - \frac{T_V}{T}\right)\right\}$$

in which the coefficient A =βP_0, β∈[0.54,0.56] and P_0 is the pressure in the atmosphere; the secondary coefficient B may be determined using the following formula: B=$\Delta H_v/RT_v$, ΔH_v was its vaporization heat. The gas constant is given here by R. and T_v is the temperature of saturation ; T is now the temperature determined by solving the aforementioned equations [51].

The energy density of the laser has a Gaussian dispersion [51]. The laser moves at a steady scanning rate throughout scan, and the ED of the beam may be described by the equation (vii):

$$\text{vii.} \quad q = \frac{2Ap}{\pi R_b^2} exp\left[-2\frac{(x-vt-x_0)^2+(y-y_0)^2}{R_b^2}\right]$$

where A represents the beam absorbance of the powder particles, p reflects beam power, R_b represents the laser's radius, v is the scanning rate. (x_0, y_0) is the original position of the laser beam center. The laser radius, R_b, is is 100 µm (same as 200 µm spot diameter which was used in the experiment).

Radiation and convection are solved for the free surface, nonetheless evaporation is considered with the consolidatiing surface [51]. So the energy equation that exists primarily on the surface of its consolidating surfaces may be written as an expression (viii):

$$\text{viii.} \quad \frac{\partial T}{\partial \vec{n}} = q - h_C(T^1 - T_0^1) - \sigma_0 \varepsilon (T^4 - T_0^4) - q_{evap}$$

where h_c is the convective heat transfer coefficient , T_0 is the surrounding temperature , The Stefan Boltzmann constant is expressed as σ_0, ε is a measurement for emissivity [51]. q_{evap} is the heat transfer caused by evaporation, and it may be expressed by the equation (ix):

$$\text{ix.} \quad q_{evap} = \omega_0 L_v = exp(2.52 + 6.121 - 18836T - 0.5logT)L_v$$

2.5. Configuration for modelling, material properties, and experimental parameters

The said theoretical framework was primarily used to simulate the HA powder production process. Its powder bed layer thickness is fixed at 100 µm (same as the experimental layer thickness). In this study, the implicit technique was employed to help solve convection, heat transport, and surface tension. Thermal properties for HA were used from the literature [53], [54]. Simulation domain which has been used is 1000 µm (length) x 600 µm (width) x 200 µm (height) in line with the experimental spot size of the laser.

Physical Properties	Value
Viscosity (g/cm/s)	2.61545 e^{-2}
Fluid Volumetric Thermal Expansion Coefficient (1/K)	2.03368 e^{-5}
Specific Heat (@ 298.15 K) erg/g/K)	5.42 e^{+06}
Reference Temperature (K)	1.08315 e^{+03}
Liquidus Temperature (K)	1.08315 e^{+03}

Solidus Temperature (K)	1.02315 e^{+03}
Latent Heat of Fusion (erg/g)	3.42538 e^{+9}
Specific Heat (@ 2073.15 K) erg/g/K)	2.34 e^{+07}
Thermal Conductivity (erg/cm/s/K)	4.68000 e^{+05}
Solid Volumetric Thermal Expansion Coefficient (1/K)	2.03368 e^{-5}
Shear Modulus (dyne/cm^2)	3.4 e^{+11}
Bulk Modulus (dyne/cm^2)	7.959 e^{+11}
Coefficient Of Solidification (Drag dyne/cm^2)	1.0 e^{+03}
Saturation Temperature (K)	3.0 e^{+03}
Density (g/cm^3)	3.08
Compressibility (cm^2/dyne)	1.0 e^{-10}
Electric Conductivity (s$Coul^2$-s/g/cm^3)	5.45498 e^{+15}
Thermal Conductivity (erg/cm/s/K)	1.0983 e^{+6}
Elastic Modulus (dyne/cm^2)	1 e^{+12}
Poisson Ratio (Unitless ratio)	4.1178 e^{-01}

2.6. Experimental procedure

Single track SLS experiments were also performed to validate the simulation model. It was created using a 3D Systems ProX® DMP 200, a fiber laser source (continuous functioning, single-mode, output at the collimator power of 300 W) with a wavelength of around 1070 nm. A 3 cm downwards laser defocus of the focal plane was used. The beam's diameter has remained steady during each single track. The laser power and speed were varied to control the amount of energy emitted while all other process parameters were kept constant. For the single track experiments, laser power four different powers were varied from 30, 36, 42, and 48W while the laser speed was kept constant at 25 mm/s. Some printed specimen have been shown in Figure 2.

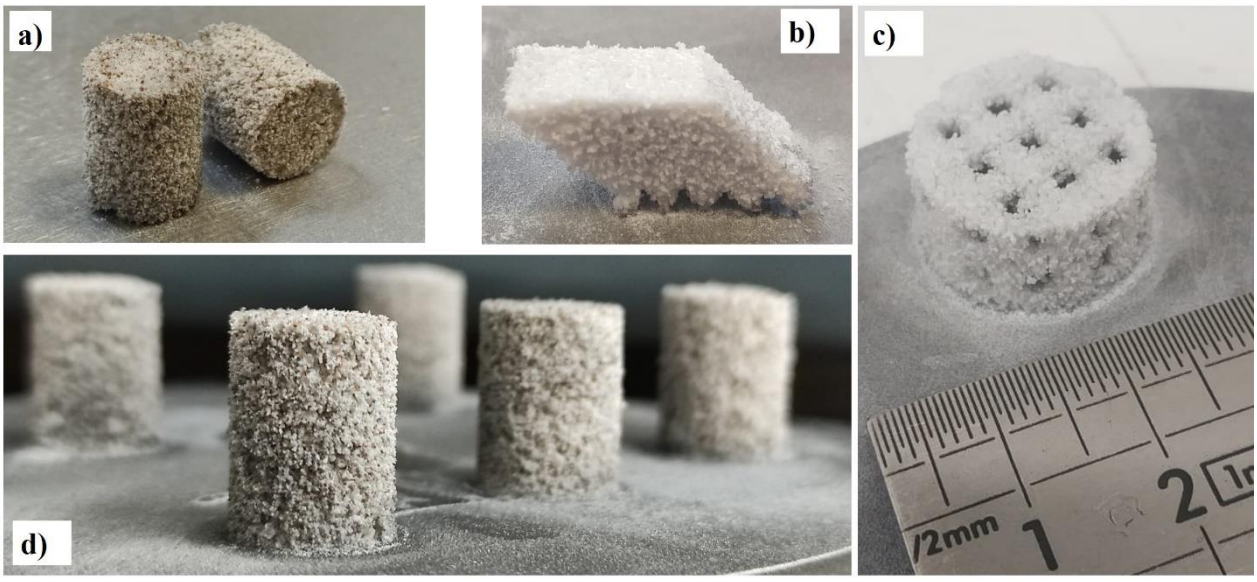

Figure 2 a) , b) and c) shows printed specimens mainly composed of HA calcium phosphate phase.

Powder and single track scanning electron micrographs were acquired using an FEI ESEM QuantaTM 450 FEG, an environmental scanning electron microscope (ESEM) equipped with a large field detector (LFD) under low vacuum (LowVac) condition but without prior metallisation of the sample's surfaces. The images were processed using ImageJ software [55]. It was necessary to apply a small layer of silver to the surfaces of the ceramic powder before using a SEM LEO 435 VP (Leica®) connected with a Ge detector (Imix-PC, PGT) in order to study the morphology and composition of the powder.

3. Results and discussion

3.1. Premature Sintering

Figure 3 a) shows the simulation domain, while the sintered zone (irradiated by laser) is shown in Figure 3 b) after magnification. Due to the low energy density, the powder particles are hardly sintered. The laser irradiation time has been marked in Figure 3 b) at 0.01s, 0.02s, and 0.032s. The laser energy density is very low for the powder to be sintered, and the interaction between the particles is also negligible.

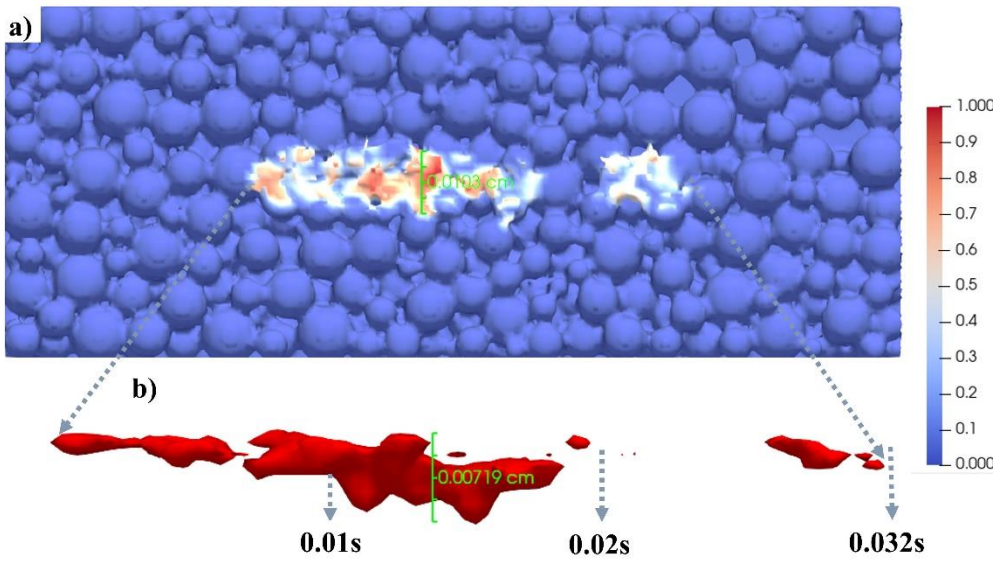

Figure 3 Premature sintering simulation with the a) laser irradiated powder bed and the b) magnified laser sintered powder zone.

Figures 4 a), b), and c) show the changed state during laser irradiation of the powder bed in the single track at 0.005, 0.0302, and 0.0492 seconds respectively, where the scale bar is showing that the red color is fully liquid state and blue is fully solid-state. It shows that there has been sintering on the powder particles but hardly any interparticle interaction to form a consistent track due to the low energy density.

Figures 4 d), e), and f) show the solid and semisolid (semisolid is the physical term for something whose state lies between a solid and a liquid) fraction under laser irradiation of the powder bed in the single track at 0.005, 0.0302, and 0.0492 seconds respectively, where the scale bar is showing that the red color corresponds to fully solid fraction and blue to fully liquid fraction. It shows that there has been

sintering only during the laser irradiation on the powder particles, but it could not retain the state after the laser passed from there.

Figures 4 g), h), and i) show the temperature gradient during and after laser irradiation of the powder bed in the single track at 0.005, 0.0302, and 0.0492 seconds, where the scale bar is showing that the red color corresponds to the highest temperature while blue to room temperature. Due to the Gaussian beam nature of the laser, the highest temperature is retained in the middle of the laser, the temperature rises very rapidly during the laser and falls very rapidly after the irradiation as shown in Figure 4 i).

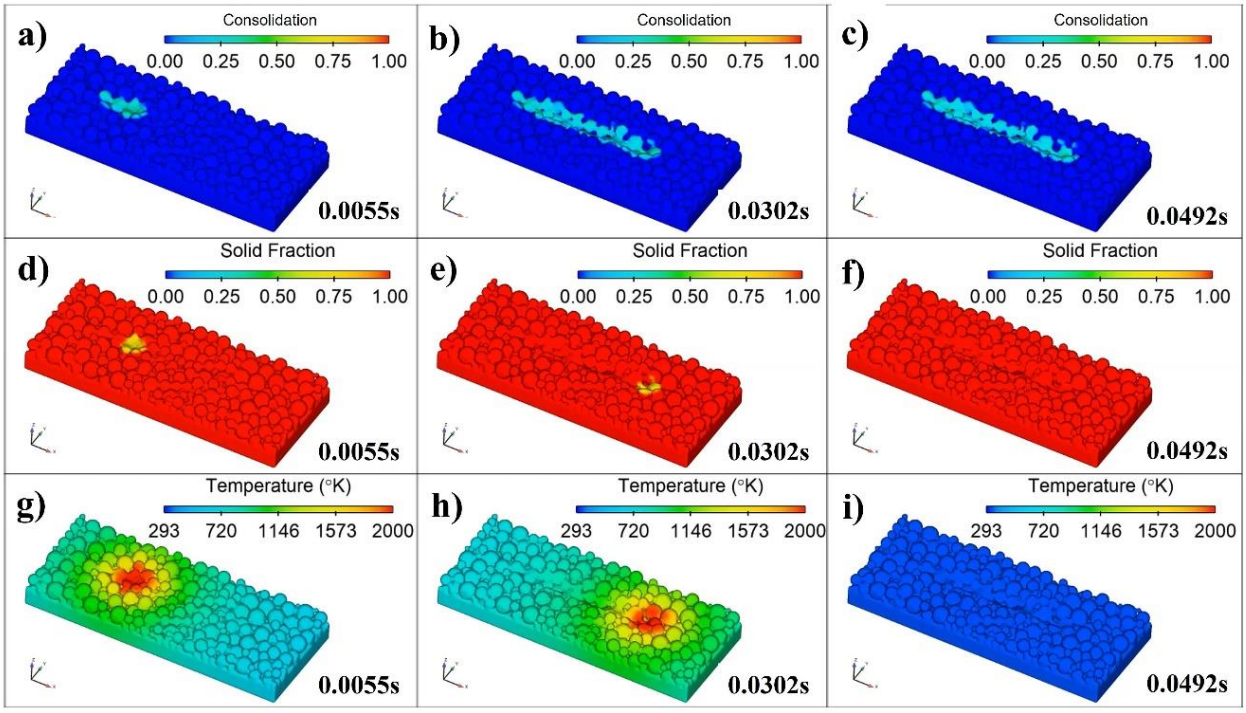

Figure 4 a), b) and c) shows the premature sintering state, d), e) and f) shows the solid fraction, g), h) and i) shows the temperature gradient, at 0.0055, 0.0302 and 0.0492 seconds respectively.

3.2. Sintering

Figure 5 a) shows the cross section of the powder particles with the state of the powder under laser where the scale bar shows 1 as fully solid and 0 as fully non-solid state on the very small region. Figure 5 b) shows the cross section of the powder particles with the temperature gradient under laser where the scale bar shows red as highest temperature and blue as the lowest temperature. While Figure 5 c) shows the top view of the sintered region and the sintered powder has been extracted in Figure 5 d) where the depth of the powder has also been shown in the figure which is around 54 micron. Which is the reason it can not stick to the baseplate since the layer thickness is around 100 microns. The scale bar in Figure 5 c) and d) is showing the interaction of the powder with laser where red color depicts full interaction and blue means no interaction at all, while the white color is showing the boundary. Similarly, Figure 5 e) shows the top view of the sintered region, and the sintered powder has been extracted in 8f where the temperature gradient can be clearly seen. The depth of the powder has also been shown in the Figure 5

c) and d) which is around 54 micron. Which is the reason it can not stick to the baseplate since the layer thickness is around 100 micron.

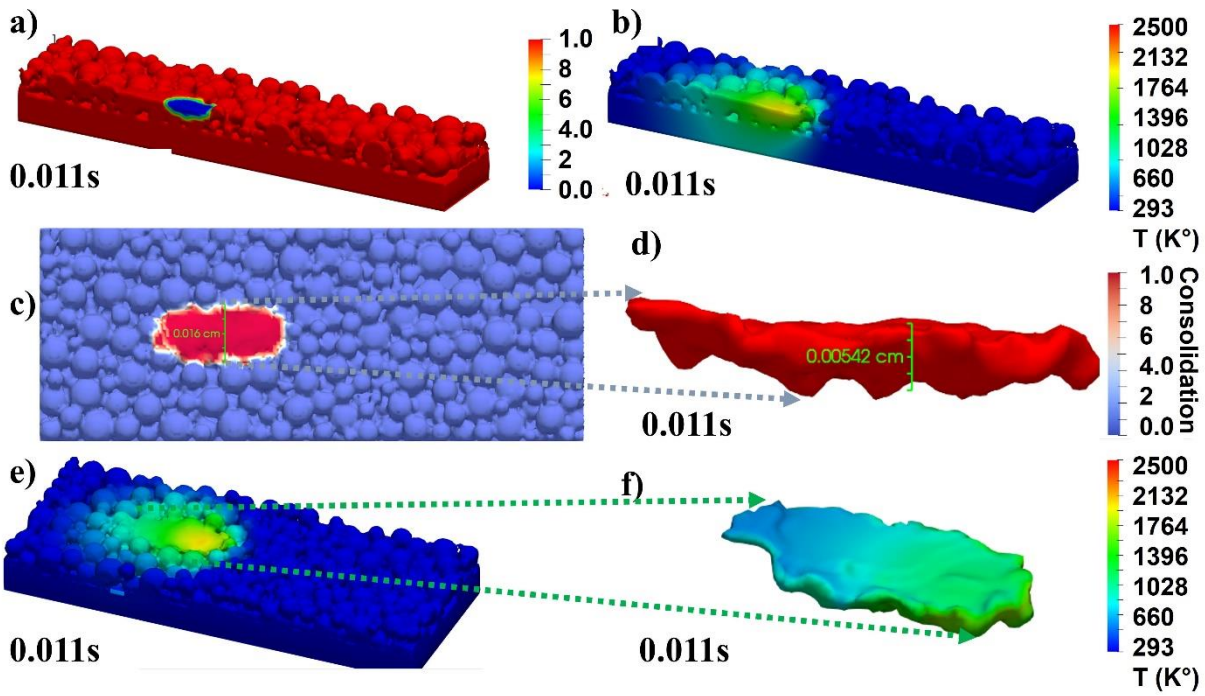

Figure 5 Sintering mode a) solid fraction, b) temperature gradient, cross sections; Sintering c) top view, d) sintered powder only; temperature gradient e) full, and f) sintered powder only.

Figure 6 a) shows the simulation domain, while the magnified laser sintered powder zone has been shown in Figure 6 b). Due to the low energy density, the powder particles are sintered to the maximum of 80-micron depth. The mechanism behind this formation can be better explained by looking at the physics behind the process shown in the next figure. The laser irradiation time has been marked in Figure 6 b) at 0.01s, 0.02s, and 0.032s. The laser energy density is low but higher than the premature sintering. The sintering depth has been increased upto 80 micron but still not enough for the 100 micron layer to be fully consolidated on the base plate.

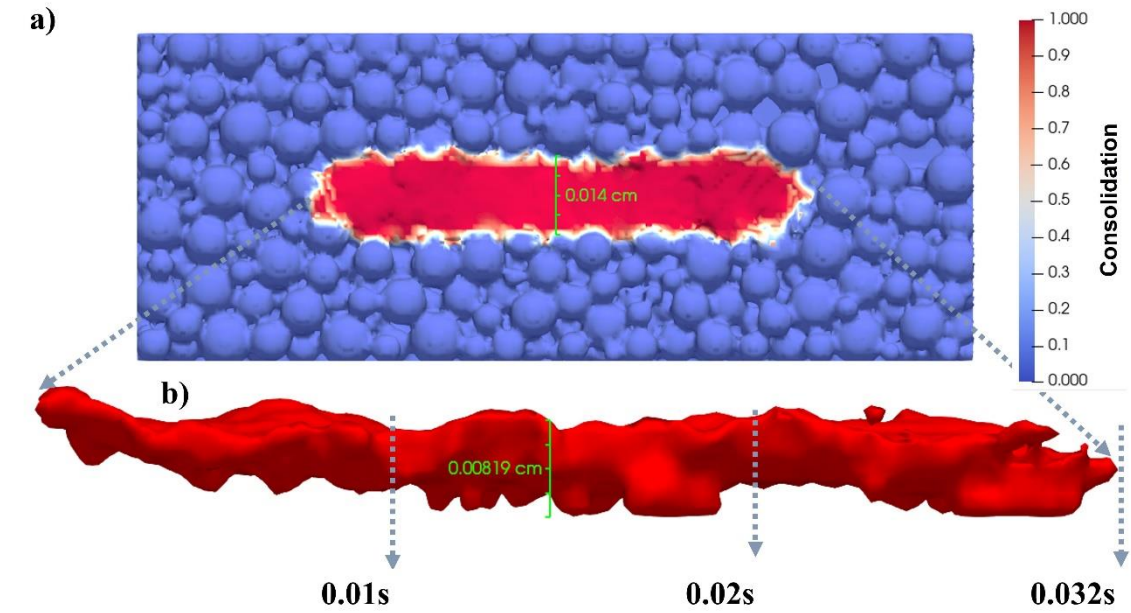

Figure 6 a) Laser irradiated powder bed and b) magnified laser sintered powder zone.

Figure 7 a) shows cumulative evaporated mass. The irradiation time is shown from 0 to 0.032s. The particles are being sintered when there is nominal evaporation along with it. When the irradiation of the laser starts at 0s the temperature rises up and after a brief interval the evaporation starts as pointed out in red circle. After 0.032s the irradiation has stopped. Figure 7 c) shows that when the irradiation starts the cooling rate increases, cooling rate continues to increase with the temperature increase (or the time of laser irradiation) even after irradiation (at 0.032s the irradiation has stopped) and normalizes itself with the surrounding temperature by the heat addition as pointed out in red circle. Figure 7 d) shows the temperature gradient. When the laser is irradiating the gradient keeps increasing the temperature gradient. However , there is a slight delay in the temperature gradient rise when the laser starts at 0.0s as pointed out by red circle. The ratio between the temperature gradient and cooling rate has been presented in Figure 7 b). The cooling rate is very slow because the irradiation area is receiving heat continuously from the adjacent area being irradiated, however, when the evaporation occurs it experiences a rapid cooling. Similarly, when the laser irradiation is stopped it also experiences a rapid cooling.

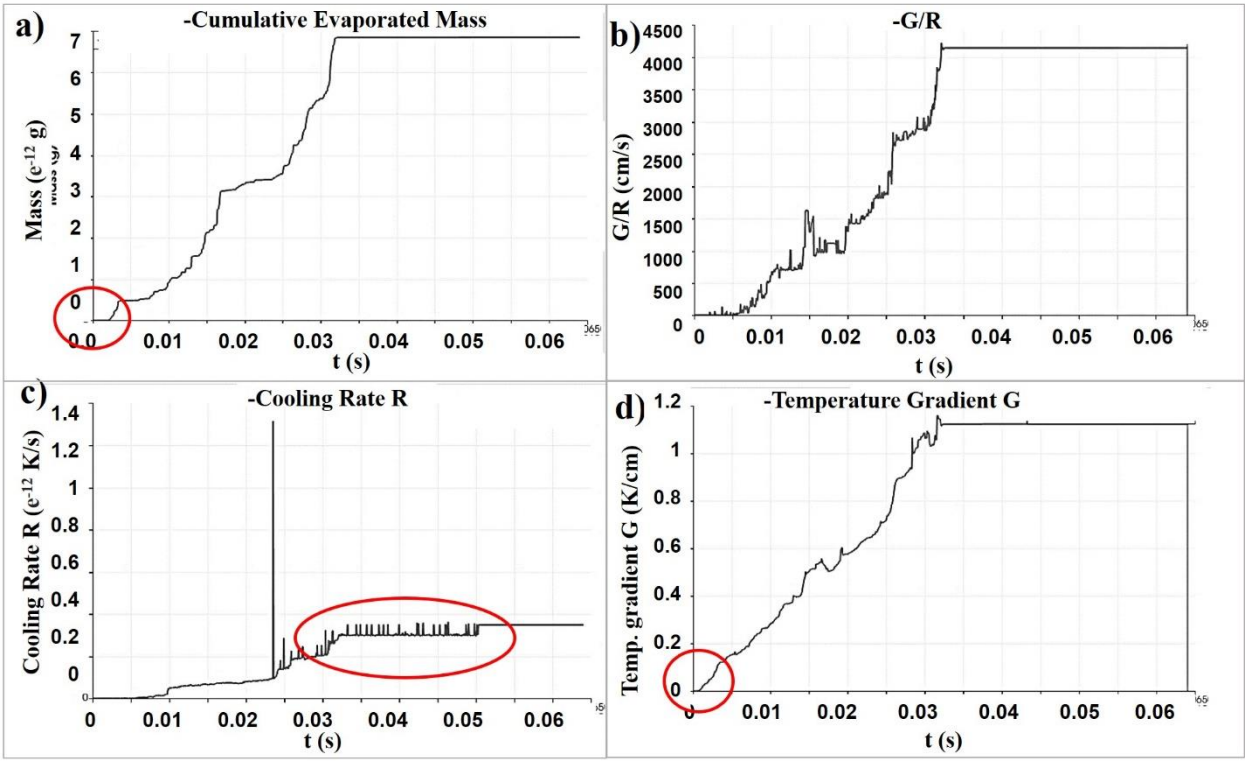

Figure 7 a) cumulative evaporated mass, b) temperature gradient G and cooling rate ratio c) cooling rate R, and d) temperature gradient

Figure 8 a) shows laser movement in x direction, while Figure 8 b) shows average and minimum temperature of the domain. The laser irradiation time is directly proportional to the average temperature increase in the process and it shows that the time of the laser irradiation increases the average temperature of the domain. Figure 8 c) shows cumulative mass of the consolidated powder which also keeps increasing with the irradiation. Figure 8 d) shows the total volume of the un-consolidated powder.

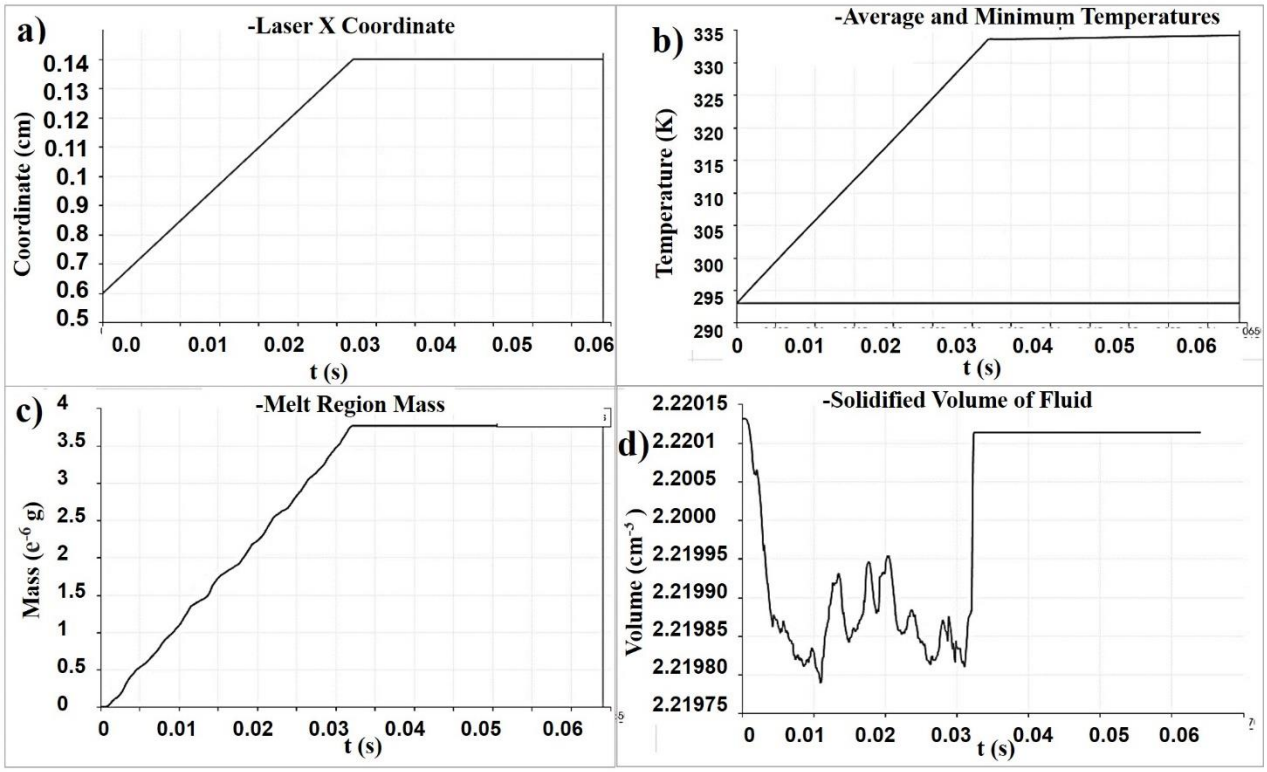

Figure 8 a) laser movement in x direction, b) average and minimum temperature of the domain, c) cumulative mass of the consolidated powder, and d) total volume of the un-consolidated powder.

Figure 9 reveals velocity-vectors during sintering and their interaction with the baseplate, corresponding at a), 0s b), 0.0055s c), 0.0150s d), 0.0220s e), 0.0302s. The velocity-vectors depict the direction of the velocity at any point under the laser.

As the laser is sintering the particles it also pushes consolidation domain downwards, the newly heated HA fuse partially with the baseplate. Same can be observed in throughout the irradiation in Figure 9 c), d) and e).

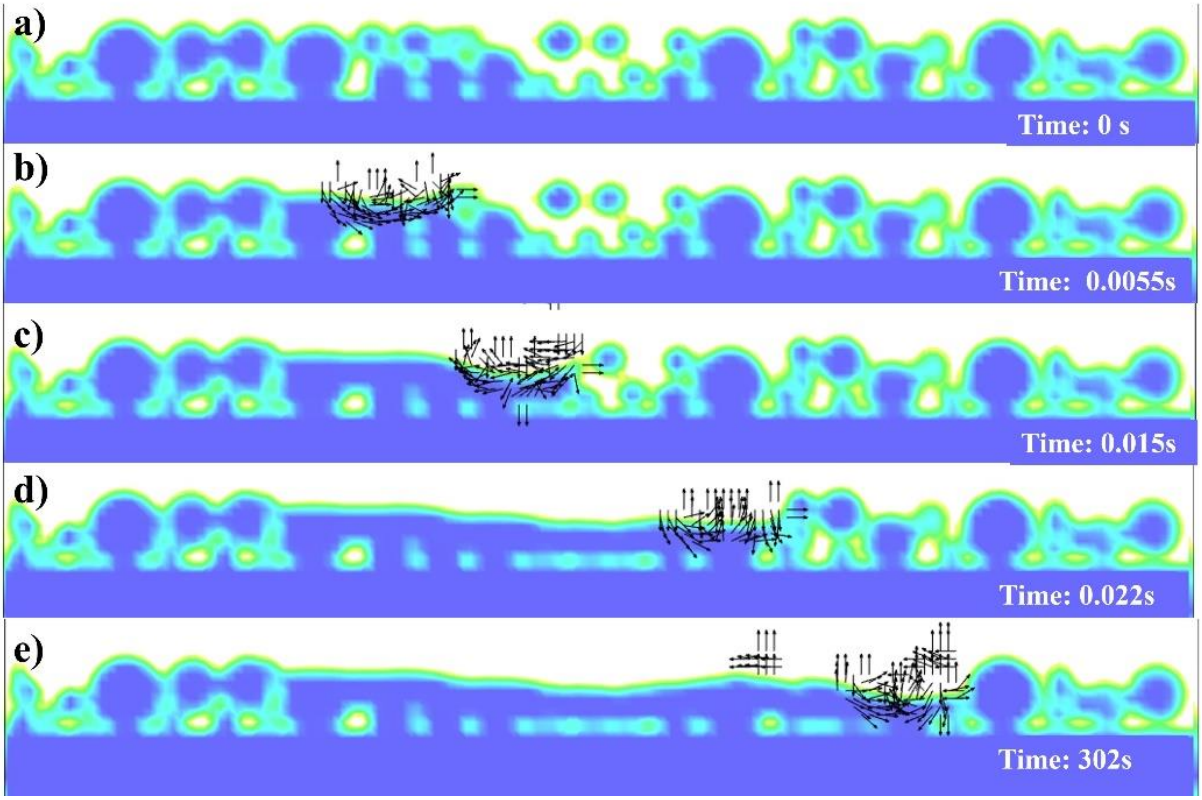

Figure 9 Velocity-vectors during sintering of the cross section at a) 0s, b) 0.0055s, c) 0.0150s, d) 0.0220s, and e) 0.0302 s.

The sintering movement for the consolidation domain from above the surface are shown in Figure 10 a) to b) under laser irradiation. Ceramics as HA, are insulators of heat which is the reason heat is not propagated very fast unlike metallic alloys [20], [24], [56]. Heat is accumulated and propagates slower which also contributes to the thermal cracks shown in Figure 10 a) to d). A tiny flow pattern under the irradiating laser can be observed.

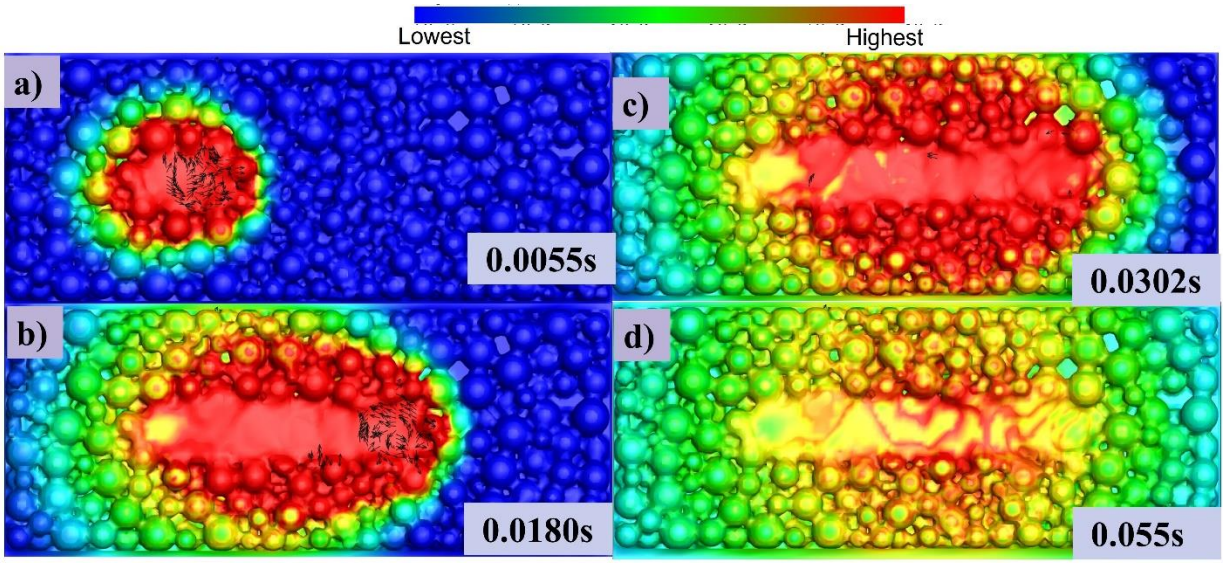

Figure 10 Heat accumulation during sintering with velocity-vectors top-view of single track at a) 0.0055, b) 0.0180s, c) 0.0302s, and d) 0.055s.

Figure 11 reveals heat accumulation in the cross sectional image, referringing to a), 0 b), 0.0055 c), 0.0180s d), 0.0302 e), 0.055 s, with velocity-vectors of the flow surrounding the consolidation region and is shown by color gradient A temperature profile is formed as the laser travels to irradiate the powder. HA is not good conductor of heat so the heat is accumulated as the laser moves which results in slower propagation of heat, unlike alloys [20], [24], [56]. Surface tension is often higher at the laser irradiating end (warm) than at the back (cold) in materials other than HA. Nonetheless, in ceramics like HA due to the low conductivity, it is dissipated from both ends and slowly accumulated to the middle.

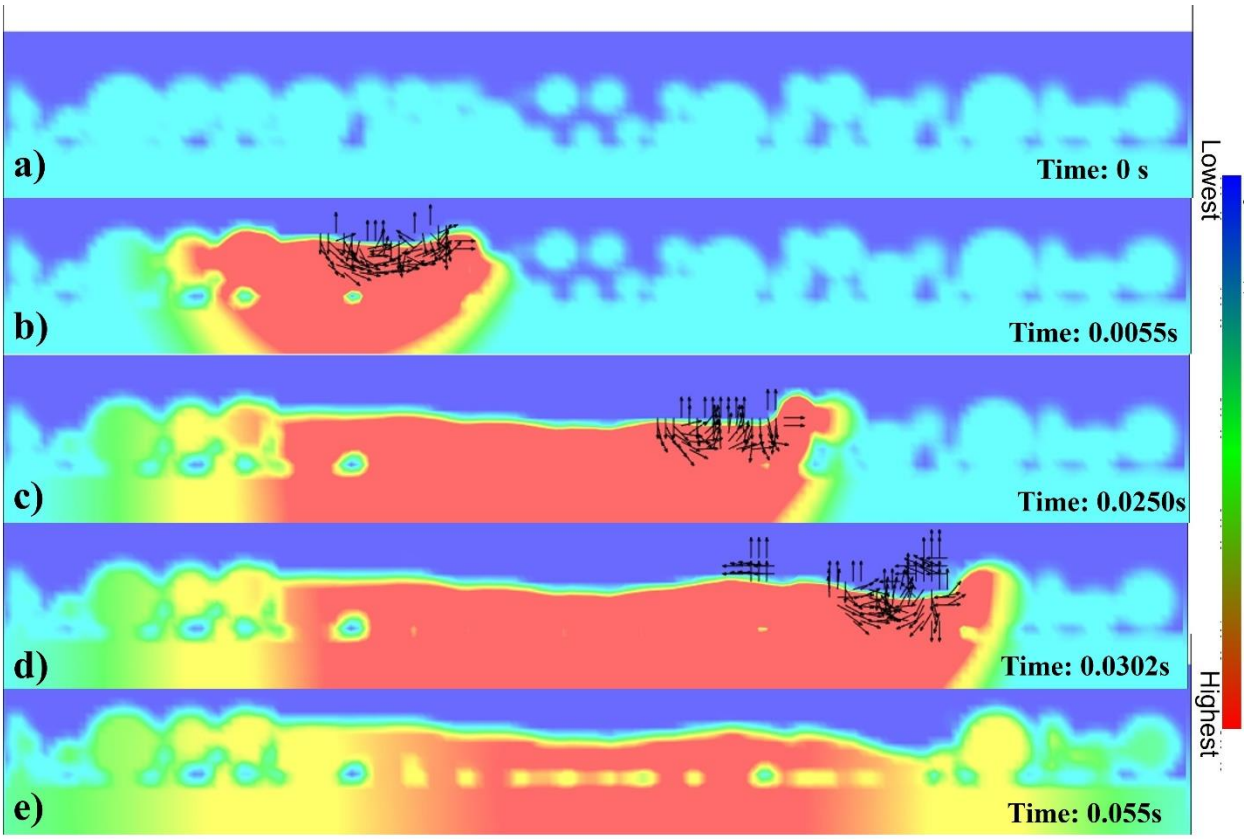

Figure 11 Heat accumulation with velocity-vectors of the cross section at a) 0s, b) 0.0055s, c) 0.0180s, d) 0.0302s, and e) 0.055s.

The density change with velocity-vectors Figure 12 depicts the views from the top. When seen from above, arrows in the consolidation domain normally trace their motions backward, although the particles influence this behavior (to be heated, tiny particles need lower ED and big particles require greater ED). They start to sinter and fuse with each other with the irradiation.

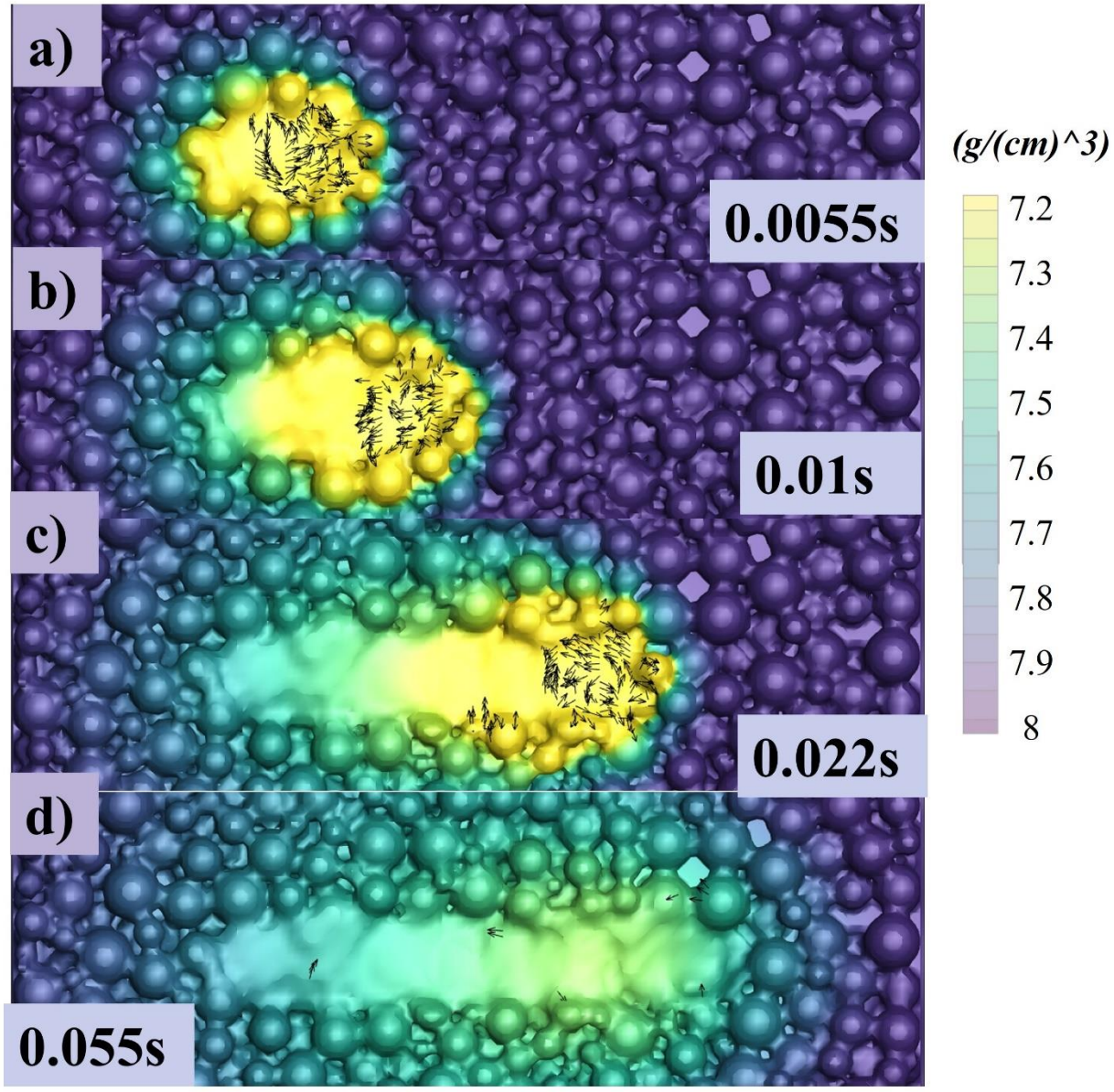

Figure 12 Top-view density change with velocity-vectors at a) 0.0055s, b) 0.01s, c) 0.022s, and d) 0.055 µs.

Figure 13 reveals temperature propagation with velocity-vectors of the movement within the consolidation domain, where the temperature of the powder bed in cross sectional view can be seen as a gradation of hue. The different images correspond to a) 0s, b) 0.0055s, c) 0.0180s, d) 0.0302s, and e) 0.055s.

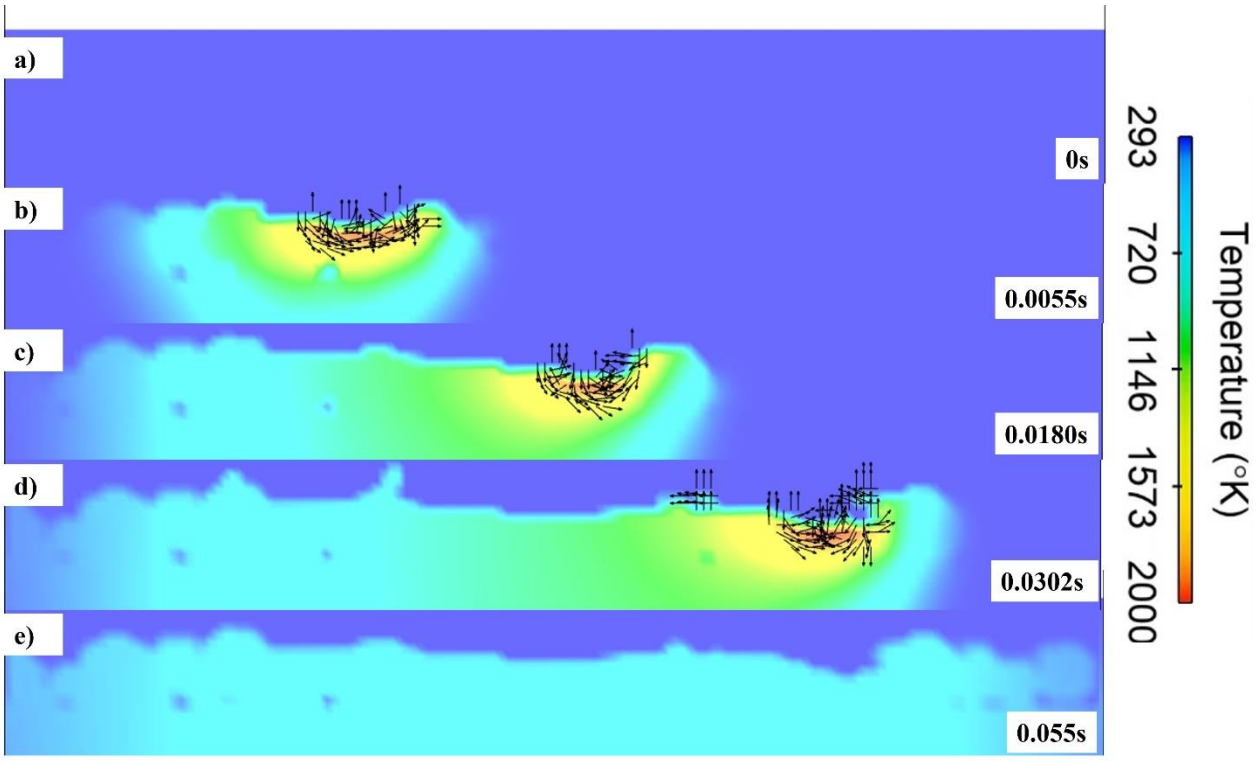

Figure 13 Temperature propagation with velocity-vectors of the cross section at a) 0s, b) 0.0055s, c) 0.0180s, d) 0.0302s, e) 0.055s.

The particle flow patterns of particles during the sintering of powder are seen from the top in Figure 14. From above, arrows trace their movements and are affected by the particles due to the already mentioned differences in ED required to heat particles of different sizes. A particle motion is therefore created with circulation flowing in opposing directions depending on the sphericity of the powder, as seen in Figure 14.

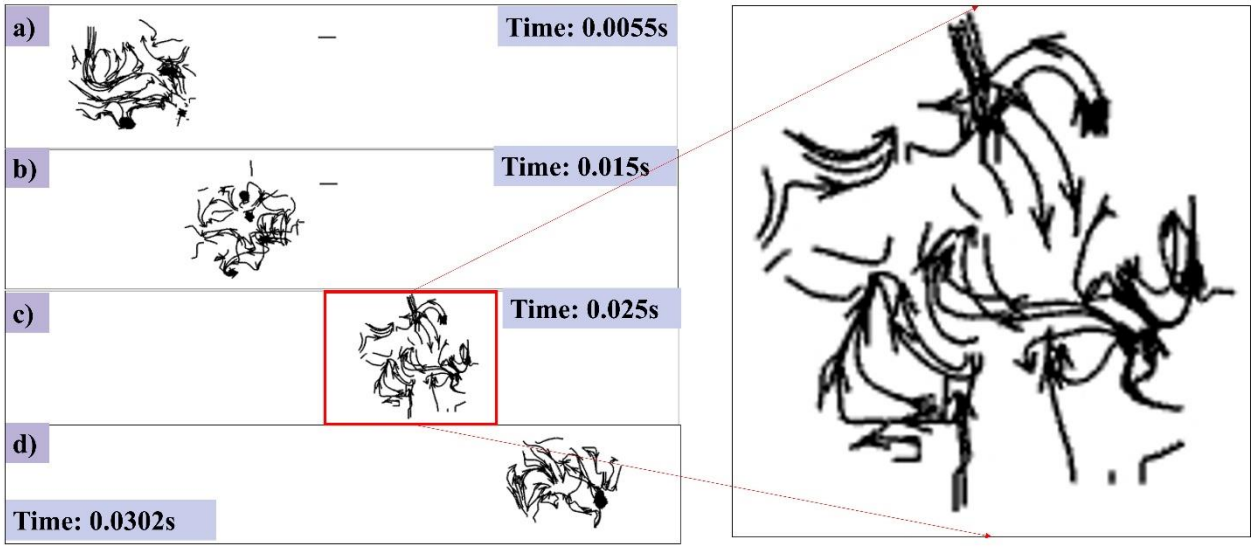

Figure 14 Top-view of stream traces during sintering at a) 0.0055s, b) 0.015s, c) 10.025s, and d) 0.0302s.

3.3. Consolidation, and Consolidation + Baseplate Consolidation

In Figure 15 the density cut off has been used, where the lowest density and the highest temperature material has been cut off from the simulation domain. It shows the material and base plate interaction, how the powder is fusing together with the base plate.

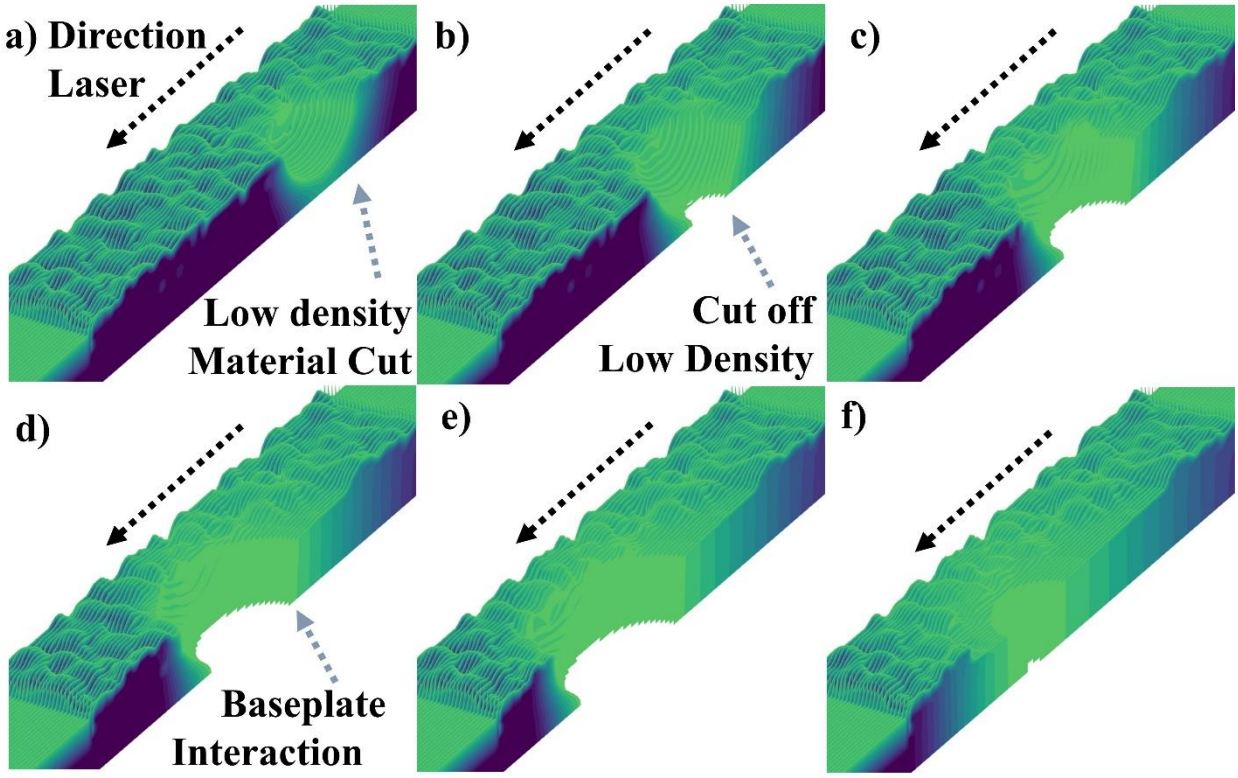

Figure 15 Base plate interaction at a), 0.001 b), 0.0055 c), 0.0180s d), 0.0202 e), 0.300 s f), 0.310s

Figure 16 reveals the solid and liquid fractions. The consolidation starts with the laser irradiation that can be seen from Figure 16 a), then the corresponding temperature field from Figure 16 e). The consolidation domain starts to grow as the heat accumulation increases in Figure 16 b) and the corresponding temperature field in Figure 16 f). As the consolidation domain keeps progressing it inconsistently interacts with the layer down below. The consolidated region exceeds the powder boundary and consolidates the baseplate in Figure 16 b) and c). After the irradiation is complete it keeps the morphology of the track as shown in Figure 16 d) and h).

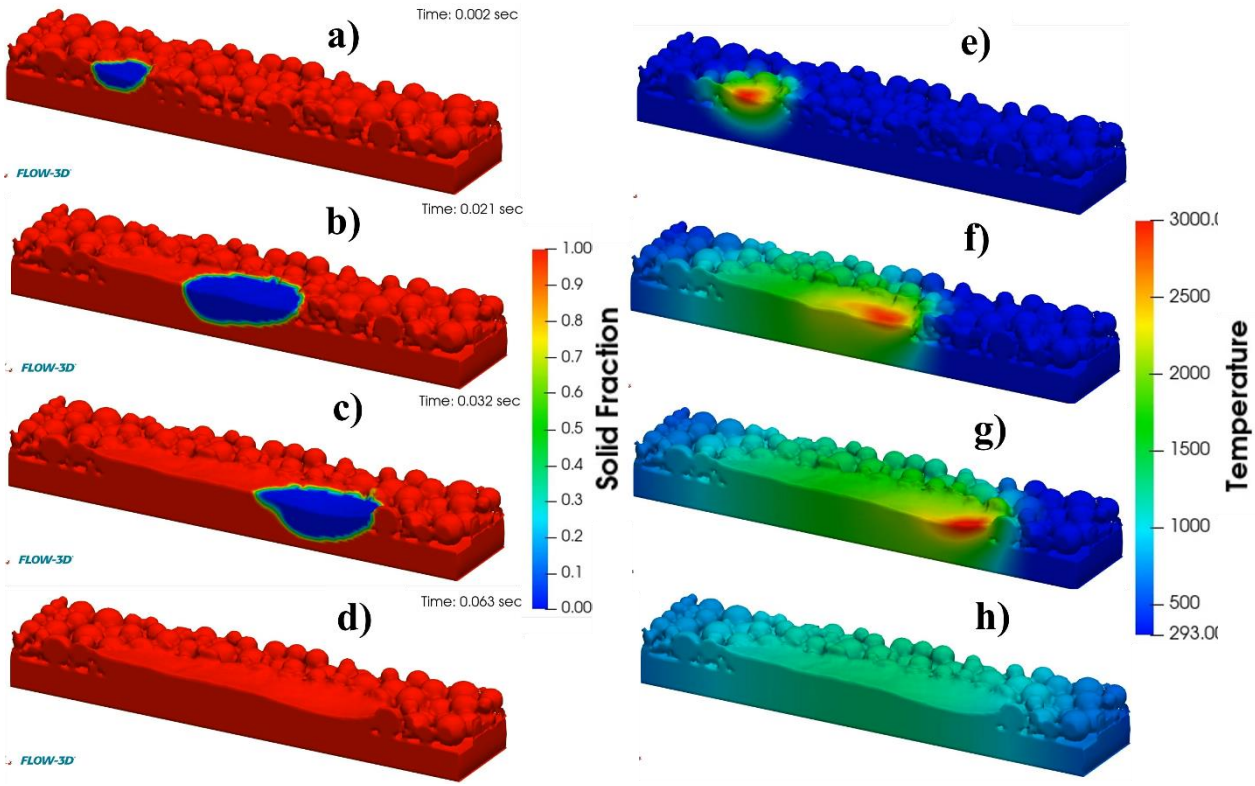

Figure 16 Solid and consolidated fraction within the cross section at a) 0.002s, b) 0.021s, c) 0.032s, and d) 0.063s. Temperature propagation within the cross section at e) 0.002s, f) 0.021s, g) 0.032s, and h) 0.063s.

Figure 17 a), b), c) and d) show the consolidation stream traces in 3D at a) 0.0055s, b) 0.015s, c) 0.025s and d) 0.0302s. The consolidation mechanism has been clearly revealed, it is showing the movement of the material from powder ad how the sintered particle fuse. As the laser heats the particles, a rapid diffusion takes place resulting in consolidation of the track. The particles consolidate themselves with the adjacent particles and due to the empty spaces the diffusion results in movement of the particles. At the start at 0.0055s the particle consolidate themselves in the random order as depicted by the sintering regime however when it gains enough heat the particle consolidation gets uniform and the consolidating particle trace their movement in the middle of the laser spot as seen in 0.015s and 0.025s. While as the laser irradiation shuts down at 0.0302s the consolidation movement becomes random with the rapid dissipation of heat.

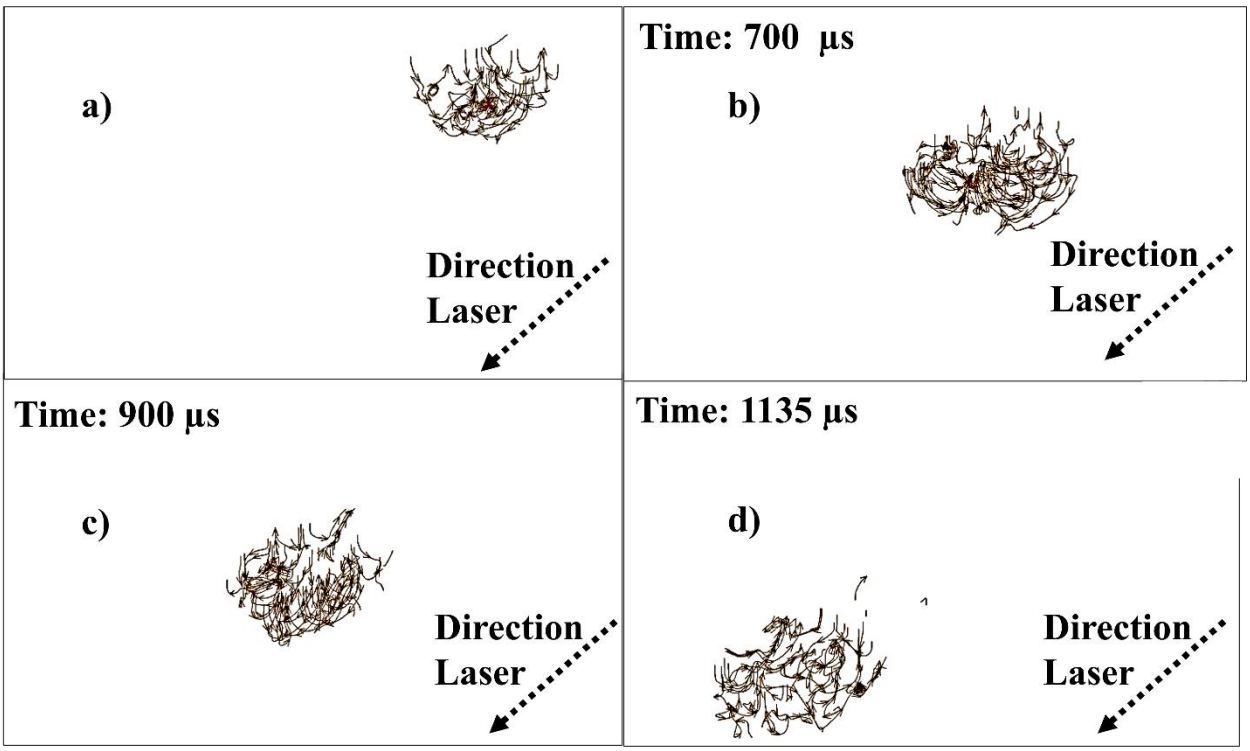

Figure 17 Velocity-vectors of single track consolidation domain in 3D at a) 0.0055s, b) 0.015s, c) 0.025s and d) 0.0302s.

Figure 18 shows the four different consolidation mechanisms occurring at different LEDs, based on the changes of laser power from (30W to 48W) and scanning speed (25mm/s). When the LED is low the powder layer is prematurely sintered, and the layer does not consolidate at all on the baseplate e.g. 30W and 25mm/s. The four consolidation regimes have been defined in the Table 1.

Table 1 comsolidation regimes and their definations

Regime	Defination
Premature sintering with no baseplate interaction	Particles can not be fused properly and ED is neither enough to form a consistent track nor it can reach the baseplate.
Sintering	Particles can be hardly fused and ED is neither enough to form a consistent track. ED is just enough for the particles to reach the layer end.
Consolidation	Particles can be fused completely and ED is enough to form a consistent track. ED is enough for the particles to reach the layer end.
Full consolidation with baseplate consolidation	Particles can be fused completely and ED is enough to form a consistent track. ED is enough for the particles to reach beyond the layer end and is able to penetrate within the base plate to resinter it with the track.

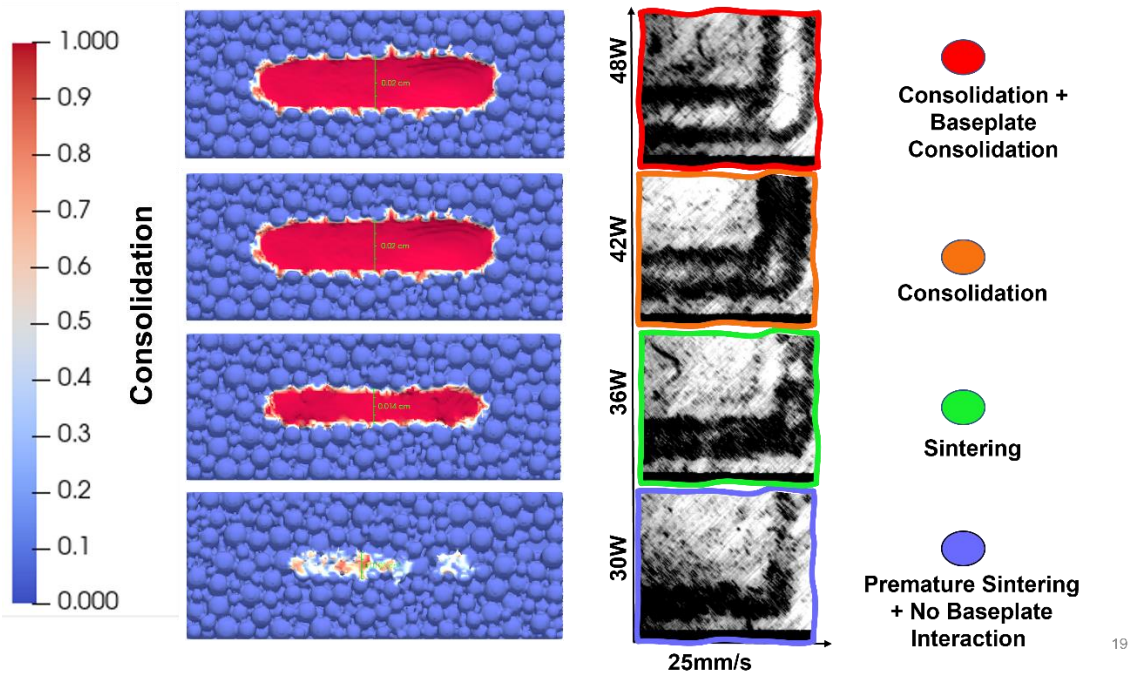

Figure 18 SEMs showing the different consolidation mechanisms: Premature Sintering + No Baseplate Interaction ; Premature Sintering; Consolidation; and Full Consolidation + Base Plate Consolidation

Figure 19 shows the model distribution of the consolidation point temperature reached in four single tracks at increasing LED. Each consolidation mechanism will be discussed in detail below.

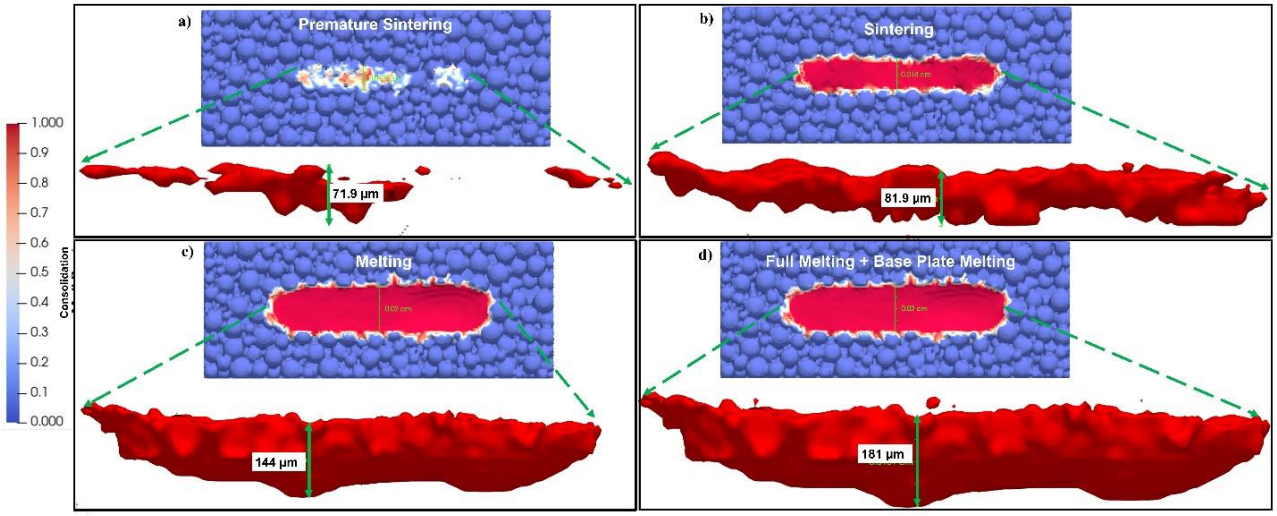

Figure 19 Simulation for different powder consolidation mechanisms: a) premature sintering with no baseplate interaction b) sintering c) consolidation and d) full consolidation with baseplate consolidation

4. Conclusions

The fundamental forming mechanisms in HA SLS were investigated systematically. In SLS, a mechanism was created for monitoring shaping behaviors across the entire regimes. On a HA-coated substrate, a high-intensity laser was employed to develop HA single tracks. A thorough examination of the functionality of LED was performed on single track creation. The geometry, morphology, and consolidation of single tracks generated at various LED levels were studied in depth. SLS shaping thermal behavior were modelled and validated by tests using a finite volume method-based model. Throughout the consolidating region, we uncovered the consolidation mechanism and studied the driving variables as well as the basic mechanisms.

The consolidation mechanism of HA material treated by SLS was revealed. The four different consolidation mechanisms were identified occurring at varying LED, based on the changes of laser power from (30W to 48W) while keeping the scanning speed (25mm/s). Following conclusions can be withdrawn:

- When LED is low the powder layer is prematurely sintered, and the layer does not consolidate at all on the baseplate e.g. 30W and 25mm/s.
- When LED is increased the powder layer is sintered, and the layer will sinter on the baseplate e.g. 36W and 25mm/s.
- When LED is increased further the powder layer is consolidated, and the layer will consolidate on the baseplate as well how ever thermal cracking leads to the cracks all over the track e.g. 42W and 25mm/s.When LED is increased even further beyond the consolidation regime the powder layer is consolidated and the baseplate is also reconsolidated, however thermal cracking will increase even further leads to the cracks all over the track. As the laser heats the particles, a rapid diffusion takes place resulting in consolidation of the track. The particle movement during consolidation is driven by the particles fusion or sintering with each other to form a consolidated region and it is also dependent on the particles under laser irradaition.

The heat penetration to baselate below the powder bed is necessary for the powder-baseplate sintering or consolidation for all regimes. Further studies on the the mechanical properties and bioactive properties can be a step forward towards the production of 3D printed HA implants.

Acknowledgments

This project has received funding from the European Union's Horizon 2020 research and innovation programme under the Marie Skłodowska-Curie grant agreement No 764935.

REFERENCES

[1] A. Ur Rehman and V. M. Sglavo, “3D printing of geopolymer-based concrete for building applications,” *Rapid Prototyp. J.*, vol. 26, no. 10, pp. 1783–1788, Sep. 2020, doi: 10.1108/RPJ-09-2019-0244.

[2] A. Ur Rehman and V. M. Sglavo, “3D printing of Portland cement-containing bodies,” *Rapid Prototyp. J.*, vol. 28, no. 2, pp. 197–203, Jan. 2022, doi: 10.1108/RPJ-08-2020-0195.

[3] M. A. Mahmood *et al.*, “Printability for additive manufacturing with machine learning: Hybrid intelligent Gaussian process surrogate-based neural network model for Co-Cr alloy,” *J. Mech. Behav. Biomed. Mater.*, vol. 135, no. July, pp. 1–11, Nov. 2022, doi: 10.1016/j.jmbbm.2022.105428.

[4] R. T. Mushtaq, A. Iqbal, Y. Wang, Q. Cheok, and S. Abbas, “Parametric Effects of Fused Filament Fabrication Approach on Surface Roughness of Acrylonitrile Butadiene Styrene and Nylon-6 Polymer,” *Materials (Basel).*, vol. 15, no. 15, p. 5206, 2022, doi: 10.3390/ma15155206.

[5] A. U. Rehman, F. Pitir, M. U. Salamci, A. Ur Rehman, F. Pitir, and M. U. Salamci, “Full-field mapping and flow quantification of melt pool dynamics in laser powder bed fusion of SS316L,” *Materials (Basel).*, vol. 14, no. 21, pp. 16–19, Oct. 2021, doi: 10.3390/ma14216264.

[6] A. U. Rehman, F. Pitir, M. U. Salamci, A. Ur Rehman, F. Pitir, and M. U. Salamci, “Laser powder bed fusion (LPBF) of In718 and the impact of pre-heating at 500 and 1000◦ C: Operando study,” *Materials (Basel).*, vol. 14, no. 21, p. 764935, Nov. 2021, doi: 10.3390/ma14216683.

[7] S. Zhang, Q. Wei, L. Cheng, S. Li, and Y. Shi, “Effects of scan line spacing on pore characteristics and mechanical properties of porous Ti6Al4V implants fabricated by selective laser melting,” *Mater. Des.*, vol. 63, pp. 185–193, 2014, doi: 10.1016/j.matdes.2014.05.021.

[8] B. Song, S. Dong, B. Zhang, H. Liao, and C. Coddet, “Effects of processing parameters on microstructure and mechanical property of selective laser melted Ti6Al4V,” *Mater. Des.*, vol. 35, pp. 120–125, Mar. 2012, doi: 10.1016/j.matdes.2011.09.051.

[9] J. J. Marattukalam *et al.*, “The effect of laser scanning strategies on texture, mechanical properties, and site-specific grain orientation in selective laser melted 316L SS,” *Mater. Des.*, vol. 193, Aug. 2020, doi: 10.1016/j.matdes.2020.108852.

[10] N. Read, W. Wang, K. Essa, and M. M. Attallah, “Selective laser melting of AlSi10Mg alloy: Process optimisation and mechanical properties development,” *Mater. Des.*, vol. 65, pp. 417–424, Jan. 2015, doi: 10.1016/j.matdes.2014.09.044.

[11] V. A. Popovich, E. V. Borisov, A. A. Popovich, V. S. Sufiiarov, D. V. Masaylo, and L. Alzina, “Impact of heat treatment on mechanical behaviour of Inconel 718 processed with tailored microstructure by selective laser melting,” *Mater. Des.*, vol. 131, pp. 12–22, 2017, doi: 10.1016/j.matdes.2017.05.065.

[12] W. Zheng *et al.*, “Fabrication of high-performance silica-based ceramic cores through selective laser sintering combined with vacuum infiltration,” *Addit. Manuf.*, vol. 48, p. 102396, Dec. 2021, doi: 10.1016/J.ADDMA.2021.102396.

[13] H. S. Maurya, K. Kosiba, K. Juhani, F. Sergejev, and K. G. Prashanth, “Effect of powder bed preheating on the crack formation and microstructure in ceramic matrix composites fabricated by laser powder-bed fusion process,” *Addit. Manuf.*, vol. 58, p. 103013, Oct. 2022, doi:

10.1016/J.ADDMA.2022.103013.

[14] S. Wu, L. Yang, C. Wang, C. Yan, and Y. Shi, “Si/SiC ceramic lattices with a triply periodic minimal surface structure prepared by laser powder bed fusion,” *Addit. Manuf.*, vol. 56, p. 102910, Aug. 2022, doi: 10.1016/J.ADDMA.2022.102910.

[15] J. Weixler, M. Zweifel, and K. Wegener, “300 fs pulsed laser ablation of Al2O3 ceramic and introduction of a predictive model,” *Mater. Des.*, vol. 217, p. 110614, May 2022, doi: 10.1016/J.MATDES.2022.110614.

[16] J. Wilkes, Y. C. Hagedorn, W. Meiners, and K. Wissenbach, “Additive manufacturing of ZrO2-Al2O3 ceramic components by selective laser melting,” *Rapid Prototyp. J.*, vol. 19, no. 1, pp. 51–57, 2013, doi: 10.1108/13552541311292736.

[17] D. Gu *et al.*, “Densification behavior, microstructure evolution, and wear performance of selective laser melting processed commercially pure titanium,” *Acta Mater.*, vol. 60, no. 9, pp. 3849–3860, May 2012, doi: 10.1016/j.actamat.2012.04.006.

[18] D. Gu and Y. Shen, “Balling phenomena in direct laser sintering of stainless steel powder: Metallurgical mechanisms and control methods,” *Mater. Des.*, vol. 30, no. 8, pp. 2903–2910, Sep. 2009, doi: 10.1016/j.matdes.2009.01.013.

[19] T. S. Jang, D. E. Kim, G. Han, C. B. Yoon, and H. Do Jung, “Powder based additive manufacturing for biomedical application of titanium and its alloys: a review,” *Biomed. Eng. Lett.*, vol. 10, no. 4, pp. 505–516, Nov. 2020, doi: 10.1007/S13534-020-00177-2/METRICS.

[20] P. Navarrete-Segado, C. Frances, M. Tourbin, C. Tenailleau, B. Duployer, and D. Grossin, “Powder bed selective laser process (sintering/melting) applied to tailored calcium phosphate-based powders,” *Addit. Manuf.*, vol. 50, p. 102542, Feb. 2022, doi: 10.1016/j.addma.2021.102542.

[21] A. Montón, M. Abdelmoula, G. Küçüktürk, F. Maury, D. Grossin, and M. Ferrato, “Experimental and numerical study for direct powder bed selective laser processing (sintering/melting) of silicon carbide ceramic,” *Mater. Res. Express*, vol. 8, no. 4, Apr. 2021, doi: 10.1088/2053-1591/ABF6FC.

[22] J. Deckers, J. P. Kruth, L. Cardon, K. Shahzad, and J. Vleugels, “Densification and geometrical assessments of alumina parts produced through indirect selective laser sintering of alumina-polystyrene composite powder,” *Stroj. Vestnik/Journal Mech. Eng.*, vol. 59, no. 11, pp. 646–661, 2013, doi: 10.5545/SV-JME.2013.998.

[23] D. Triantafyllidis, L. Li, and F. H. Stott, “Crack-free densification of ceramics by laser surface treatment,” *Surf. Coatings Technol.*, vol. 201, no. 6, pp. 3163–3173, Dec. 2006, doi: 10.1016/J.SURFCOAT.2006.06.032.

[24] D. Grossin *et al.*, “A review of additive manufacturing of ceramics by powder bed selective laser processing (sintering / melting): Calcium phosphate, silicon carbide, zirconia, alumina, and their composites,” *Open Ceram.*, vol. 5, Mar. 2021, doi: 10.1016/J.OCERAM.2021.100073.

[25] B. H. Bae, J. W. Lee, J. M. Cha, I. W. Kim, H. Do Jung, and C. B. Yoon, “Preliminary Characterization of Glass/Alumina Composite Using Laser Powder Bed Fusion (L-PBF) Additive Manufacturing,” *Mater. 2020, Vol. 13, Page 2156*, vol. 13, no. 9, p. 2156, May 2020, doi: 10.3390/MA13092156.

[26] P. Navarrete-Segado, C. Frances, D. Grossin, and M. Tourbin, “Tailoring hydroxyapatite microspheres by spray-drying for powder bed fusion feedstock,” *Powder Technol.*, p. 117116, Jan.

2022, doi: 10.1016/j.powtec.2022.117116.

[27] N. K. Tolochko, T. Laoui, Y. V. Khlopkov, S. E. Mozzharov, V. I. Titov, and M. B. Ignatiev, “Absorptance of powder materials suitable for laser sintering,” *Rapid Prototyp. J.*, vol. 6, no. 3, pp. 155–160, 2000, doi: 10.1108/13552540010337029.

[28] Q. Liu, Y. Danlos, B. Song, B. Zhang, S. Yin, and H. Liao, “Effect of high-temperature preheating on the selective laser melting of yttria-stabilized zirconia ceramic,” *J. Mater. Process. Technol.*, vol. 222, pp. 61–74, 2015, doi: 10.1016/j.jmatprotec.2015.02.036.

[29] G. Urruth, D. Maury, C. Voisin, V. Baylac, and D. Grossin, “Powder bed selective laser processing (sintering / melting) of Yttrium Stabilized Zirconia using carbon-based material (TiC) as absorbance enhancer,” *J. Eur. Ceram. Soc.*, vol. 42, no. 5, pp. 2381–2390, May 2022, doi: 10.1016/J.JEURCERAMSOC.2021.12.042.

[30] H. Yves-Christian, W. Jan, M. Wilhelm, W. Konrad, and P. Reinhart, “Net shaped high performance oxide ceramic parts by Selective Laser Melting,” in *Physics Procedia*, Elsevier B.V., 2010, pp. 587–594. doi: 10.1016/j.phpro.2010.08.086.

[31] A. Ur Rehman *et al.*, “Influence of Silicon Carbide on Direct Powder Bed Selective Laser Process (Sintering/Melting) of Alumina,” *Materials (Basel).*, vol. 15, no. 2, p. 637, Jan. 2022, doi: 10.3390/ma15020637.

[32] K. Zhang, T. Liu, W. Liao, C. Zhang, Y. Yan, and D. Du, “Influence of laser parameters on the surface morphology of slurry-based Al2O3 parts produced through selective laser melting,” *Rapid Prototyp. J.*, vol. 24, no. 2, pp. 333–341, 2018, doi: 10.1108/RPJ-12-2016-0201.

[33] H. Liu *et al.*, “Direct formation of Al2O3/GdAlO3/ZrO2 ternary eutectic ceramics by selective laser melting: Microstructure evolutions,” *J. Eur. Ceram. Soc.*, vol. 38, no. 15, pp. 5144–5152, Dec. 2018, doi: 10.1016/j.jeurceramsoc.2018.07.040.

[34] S. M. H. Hojjatzadeh *et al.*, “Pore elimination mechanisms during 3D printing of metals,” *Nat. Commun.*, vol. 10, no. 1, p. 3088, Dec. 2019, doi: 10.1038/s41467-019-10973-9.

[35] Q. Guo *et al.*, “Transient dynamics of powder spattering in laser powder bed fusion additive manufacturing process revealed by in-situ high-speed high-energy x-ray imaging,” *Acta Mater.*, vol. 151, pp. 169–180, Jun. 2018, doi: 10.1016/j.actamat.2018.03.036.

[36] Q. Guo *et al.*, “In-situ characterization and quantification of melt pool variation under constant input energy density in laser powder bed fusion additive manufacturing process,” *Addit. Manuf.*, vol. 28, pp. 600–609, Aug. 2019, doi: 10.1016/j.addma.2019.04.021.

[37] H. Ghasemi-Tabasi *et al.*, “Direct observation of crack formation mechanisms with operando Laser Powder Bed Fusion X-ray imaging,” *Addit. Manuf.*, vol. 51, p. 102619, Mar. 2022, doi: 10.1016/J.ADDMA.2022.102619.

[38] T. D. Ngo, A. Kashani, G. Imbalzano, K. T. Q. Nguyen, and D. Hui, “Additive manufacturing (3D printing): A review of materials, methods, applications and challenges,” *Compos. Part B Eng.*, vol. 143, pp. 172–196, Jun. 2018, doi: 10.1016/j.compositesb.2018.02.012.

[39] E. Maire and P. J. Withers, “Quantitative X-ray tomography,” *International Materials Reviews*, vol. 59, no. 1. pp. 1–43, Jan. 2014. doi: 10.1179/1743280413Y.0000000023.

[40] P. Wang, Y. Yang, and N. S. Moghaddam, “Process modeling in laser powder bed fusion towards

defect detection and quality control via machine learning: The state-of-the-art and research challenges," *J. Manuf. Process.*, vol. 73, pp. 961–984, Jan. 2022, doi: 10.1016/J.JMAPRO.2021.11.037.

[41] T. S. Jang *et al.*, "Topography-Supported Nanoarchitectonics of Hybrid Scaffold for Systematically Modulated Bone Regeneration and Remodeling," *Adv. Funct. Mater.*, vol. 32, no. 51, p. 2206863, Dec. 2022, doi: 10.1002/ADFM.202206863.

[42] J. Baek *et al.*, "Synthesis and evaluation of bone morphogenetic protein (BMP)-loaded hydroxyapatite microspheres for enhanced bone regeneration," *Ceram. Int.*, vol. 42, no. 6, pp. 7748–7756, May 2016, doi: 10.1016/J.CERAMINT.2016.01.189.

[43] S. M. Kim *et al.*, "Enhanced Bioactivity of Micropatterned Hydroxyapatite Embedded Poly(L-lactic) Acid for a Load-Bearing Implant," *Polym. 2020, Vol. 12, Page 2390*, vol. 12, no. 10, p. 2390, Oct. 2020, doi: 10.3390/POLYM12102390.

[44] J. H. Ahn *et al.*, "3D-printed biodegradable composite scaffolds with significantly enhanced mechanical properties via the combination of binder jetting and capillary rise infiltration process," *Addit. Manuf.*, vol. 41, p. 101988, May 2021, doi: 10.1016/J.ADDMA.2021.101988.

[45] S. Eosoly, D. Brabazon, S. Lohfeld, and L. Looney, "Selective laser sintering of hydroxyapatite/poly-ε-caprolactone scaffolds," *Acta Biomater.*, vol. 6, no. 7, pp. 2511–2517, Jul. 2010, doi: 10.1016/j.actbio.2009.07.018.

[46] L. Hao, M. M. Savalani, Y. Zhang, K. E. Tanner, R. J. Heath, and R. A. Harris, "Characterization of selective laser-sintered hydroxyapatite-based biocomposite structures for bone replacement," *Proc. R. Soc. A Math. Phys. Eng. Sci.*, vol. 463, no. 2084, pp. 1857–1869, Aug. 2007, doi: 10.1098/rspa.2007.1854.

[47] R. T. Mushtaq, A. Iqbal, Y. Wang, A. M. Khan, and M. S. Abu Bakar, "Parametric optimization of 3D printing process hybridized with laser-polished PETG polymer," *Polym. Test.*, vol. 125, p. 108129, Aug. 2023, doi: 10.1016/J.POLYMERTESTING.2023.108129.

[48] R. T. Mushtaq, Y. Wang, A. M. Khan, M. Rehman, X. Li, and S. Sharma, "A post-processing laser polishing method to improve process performance of 3D printed new Industrial Nylon-6 polymer," *J. Manuf. Process.*, vol. 101, pp. 546–560, Sep. 2023, doi: 10.1016/J.JMAPRO.2023.06.019.

[49] R. Donate, M. Monzón, and M. E. Alemán-Domínguez, "Additive manufacturing of PLA-based scaffolds intended for bone regeneration and strategies to improve their biological properties," *E-Polymers*, vol. 20, no. 1, pp. 571–599, Jan. 2020, doi: 10.1515/epoly-2020-0046.

[50] H. Zeng *et al.*, "Indirect selective laser sintering-printed microporous biphasic calcium phosphate scaffold promotes endogenous bone regeneration via activation of ERK1/2 signaling," *Biofabrication*, vol. 12, no. 2, p. 025032, Mar. 2020, doi: 10.1088/1758-5090/ab78ed.

[51] Y. Tian, L. Yang, D. Zhao, Y. Huang, and J. Pan, "Numerical analysis of powder bed generation and single track forming for selective laser melting of SS316L stainless steel," *J. Manuf. Process.*, vol. 58, pp. 964–974, Oct. 2020, doi: 10.1016/j.jmapro.2020.09.002.

[52] Y. S. Lee and W. Zhang, "Modeling of heat transfer, fluid flow and solidification microstructure of nickel-base superalloy fabricated by laser powder bed fusion," *Addit. Manuf.*, vol. 12, pp. 178–188, Oct. 2016, doi: 10.1016/j.addma.2016.05.003.

[53] G. L. Hovis *et al.*, “Thermal expansion of fluorapatite-hydroxylapatite crystalline solutions,” *Am. Mineral.*, vol. 99, no. 11–12, pp. 2171–2175, 2014, doi: 10.2138/am-2014-4914.

[54] Z. El Hallaoui, T. Moudakkar, S. Vaudreuil, T. Bounahmidi, and S. Abderafi, “Experimental Investigation of Thermal Conductivity and Specific Heat of the Calcium Phosphate Ore for a Drying Application,” *Math. Probl. Eng.*, vol. 2020, 2020, doi: 10.1155/2020/4163206.

[55] C. A. Schneider, W. S. Rasband, and K. W. Eliceiri, “NIH Image to ImageJ: 25 years of image analysis,” *Nature Methods*, vol. 9, no. 7. pp. 671–675, Jul. 2012. doi: 10.1038/nmeth.2089.

[56] A. Aramian, S. M. J. Razavi, Z. Sadeghian, and F. Berto, “A review of additive manufacturing of cermets,” *Addit. Manuf.*, vol. 33, 2020, doi: 10.1016/j.addma.2020.101130.